



Harnessing manufacturing elements to select local process parameters for metal additive manufacturing: A case study on a superconducting solenoid coil

Julian Ferchow^{a,*}, Manuel Biedermann^b, Pascal Müller^b, Bernhard Auchmann^c, André Brem^d, Mirko Meboldt^b

^a Inspire AG, ipd|z, Leonhardstrasse 21, 8092 Zurich, Switzerland

^b ETH Zürich, pd|z, Leonhardstrasse 21, 8092 Zurich, Switzerland

^c Paul Scherrer Institute, Forschungsstrasse 111, 5232 Villigen, Switzerland

^d ETH Zürich, Soft Materials, Vladimir-Prelog-Weg 1-5/10, 8093 Zurich, Switzerland

ARTICLE INFO

Keywords:

Design for additive manufacturing
Laser-based powder bed fusion
Manufacturing element
Process parameter
Adhesion
Superconducting solenoid coil
Winding former

ABSTRACT

In additive manufacturing (AM), low geometrical tolerances, high-quality material properties, and low surface roughness are challenges. To increase the process capabilities, a promising concept is to tailor process parameters for the fabrication of a part. Instead of selecting identical process parameters to the geometry of the whole part, different sets of process parameters are assigned to different regions named manufacturing elements (MEs). The ME approach offers three main advantages: significant reduction of required sacrificial support structures based on the reduced build angles and less post-processing efforts; reduced AM processing time due to less sacrificial support structures and a higher laser speed; and local adjustment of the material and surface properties. Previous studies have examined the ME approach and applied it to simplified test samples. This study shows an end-to-end implementation of the ME approach for the fabrication of a real-world industrial part and highlights the associated opportunities and challenges for the implementation. The application is demonstrated for a complex-shaped industrial part that can only be manufactured using the ME approach. The industrial part is a winding former of a superconducting solenoid coil. The implementation consists of three major steps: (1) the development of a process parameter model for laser-based powder bed fusion (L-PBF) and stainless steel 316 L; (2) segmentation of the part into MEs; and (3) use of the enhanced design freedom for surface texturing. The ME approach facilitated support-free fabrication of the part with build angles of as low as 25°. The enhanced design freedom enabled surface texturing, which allowed the maximum shear strength to be improved by 63% compared to that of a nontextured surface. The results are discussed, and possible enhancements and research directions are outlined, such as the automated assignment of process parameter sets. The results are applicable to reduce the costs of a superconducting solenoid coil for the treatment of cancer with proton beams. This can enable a larger number of patients to have access to this cancer treatment. In addition, the results are further applicable to increase the performance of the future circular collider at CERN.

1. Introduction

Laser-based powder bed fusion (L-PBF) is a layer-based additive manufacturing (AM) process that enables the fabrication at reduced costs and short lead times of complex-shaped and customized metal parts, which may not be possible with conventional manufacturing

processes [1]. Despite these advantages, industrial applications of L-PBF are still limited. One challenge is the increased costs for the post-processing of parts [2,3], particularly the removal of sacrificial support structures [4]. In certain cases the removal is not even possible due to geometrical reasons. Support structures are required during fabrication but must be removed from the produced part, which is a

Abbreviations: AM, Additive manufacturing; CAD, Computer-aided design; CCT, Canted cosine theta; FCC, Future Circular Collider; FDM, Fused deposition modeling; ME, Manufacturing elements.

* Correspondence to: Inspire AG, Leonhardstrasse 21, 8092 Zurich, Switzerland.

E-mail address: ferchow@inspire.ethz.ch (J. Ferchow).

<https://doi.org/10.1016/j.addma.2021.102140>

Available online 14 July 2021

2214-8604/© 2021 The Authors. Published by Elsevier B.V. This is an open access article under the CC BY license (<http://creativecommons.org/licenses/by/4.0/>).

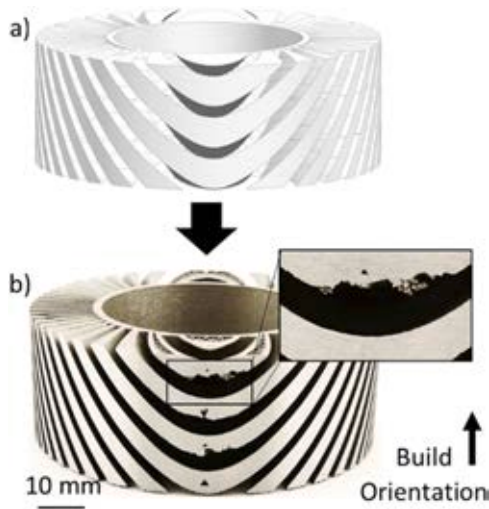


Fig. 1. Winding former of a superconducting solenoid coil: (a) computer-aided design (CAD) model; (b) winding former manufactured by laser-based powder bed fusion (L-PBF) with standard parameters and without support structures to show dross formation at overhangs, even after post-processing.

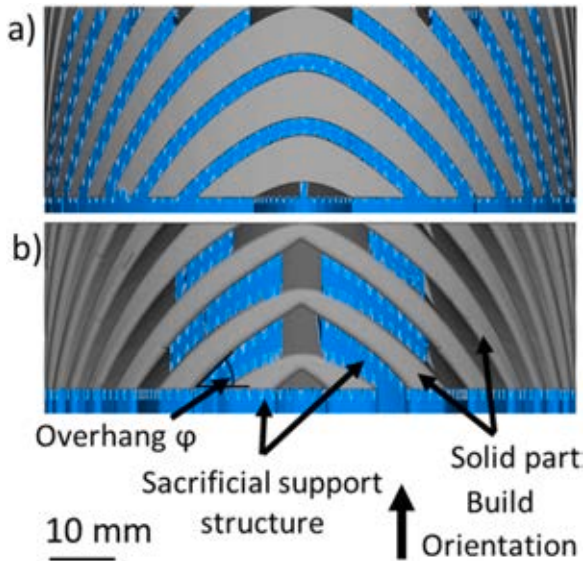


Fig. 2. (a) Ideal design of the winding former with support structures at overhangs; (b) optimized design of the winding former with a reduced amount of support structures.

manual process and can be time-consuming [5]. In the case of L-PBF, sacrificial support structures are required to dissipate heat from the local melt pool through the solid material to the base plate. Different approaches exist for this purpose [6,7]. The support is required to stabilize the solid structure and to avoid thermal warping of the part [8]. In the case of overhangs, a lack of support structures can increase the melt pool size, which leads to a rough surface with dross formations and partly molten powder particles [9]. As an example, Fig. 1(a) shows a complex-shaped L-PBF part that has overhangs with respect to the marked build orientation. The part is a section of a winding former for a tilted superconducting solenoid coil used in a particle accelerator magnet [10]. The background and detailed explanation of the winding former can be found in Section 2. Fig. 1(b) depicts the dross formation and form deviations that occur at the overhangs. Various frameworks are available to evaluate the manufacturability of L-PBF parts to take advantage of the full design capability [11,12]. However, proper fabrication of the complex-shaped winding former using L-PBF still requires support structures to be placed at these critical overhangs, as shown in Fig. 2(a). The shape can be optimized according to AM design guidelines to reduce but not eliminate the support structures, as shown in Fig. 2(b). However, when these support structures are placed in areas with limited accessibility, their removal may not be possible or very labor-intensive [13].

To avoid support structures, a common approach is to adhere to design rules that account for the specific limitations of AM processes [14,15]. For L-PBF, using standard process parameters allows design elements to be fabricated without additional support structures if they possess a minimum required build angle of $\varphi = 35\text{--}45^\circ$ and a maximum diameter $\varnothing = 9\text{--}12$ mm for circular cross-sections that are aligned horizontally to the build plate [14]. If these design rules are not satisfied, a possible solution is to modify the shape of the design element to minimize support structures. As shown in Fig. 2(b), the shape of the arches can be modified to reduce the amount of supports. However, modifying the part's geometry while using standard process parameters and AM design guidelines still requires internal supports with reduced accessibility. This problem remains even if the build orientation of the part is adjusted.

A number of prior studies have focused on increasing the capabilities of L-PBF by optimizing the process parameters to achieve build angles of less than $\varphi = 35^\circ$ [16–23]. The adjusted process parameters include the laser power, laser speed, and hatch distance, which affect the volumetric energy density E_{vd} at the local melt pool. Reducing E_{vd} minimizes the accumulated heat at the melt pool and decreases thermal stress and warpage due to insufficient heat conduction to the build plate, which allows design elements with lower overhang angles compared with standard E_{vd} . However, reducing E_{vd} also reduces the relative material density ρ_{rel}^* and mechanical strength. The dimensionless relative material density ρ_{rel}^* is the ratio between the density determined by the Archimedes measurement [24], and the theoretical reference value of stainless steel 316 L, $\rho_{ref,316L} = 7.95 \text{ g/cm}^3$. Several studies have

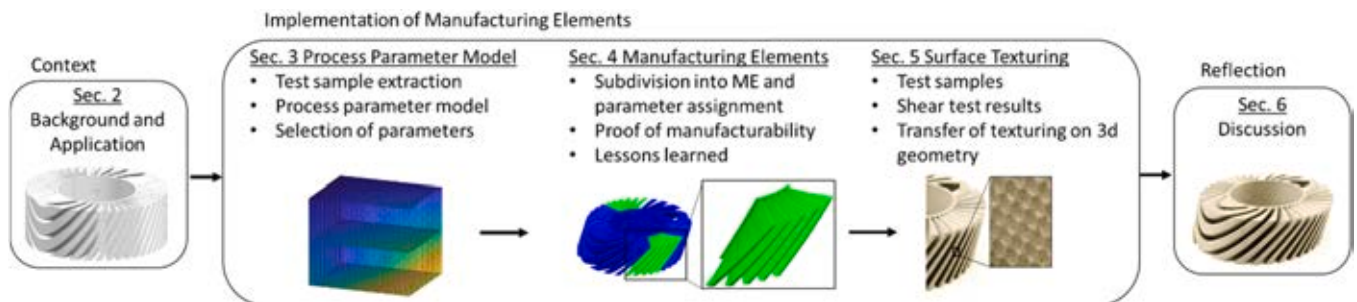


Fig. 3. Overview of this work.

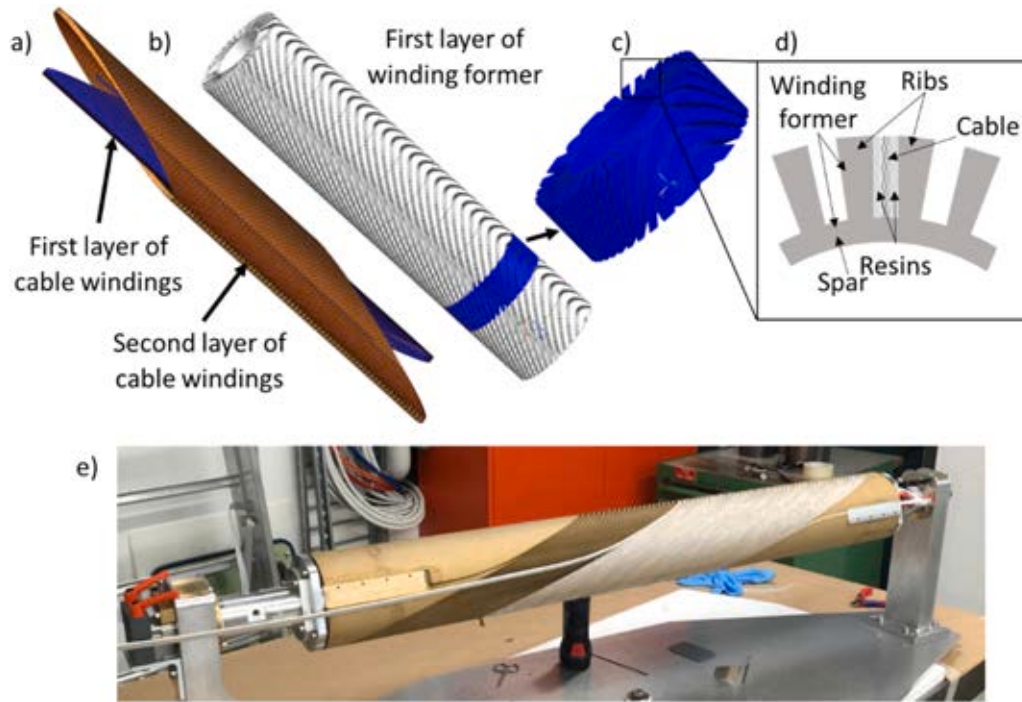


Fig. 4. Canted cosine theta coil: (a) two layers of cable windings, (b) layer of the winding former, (c) winding former section, (d) section of the composite assembly, and (e) winding former with cables on a test bench.

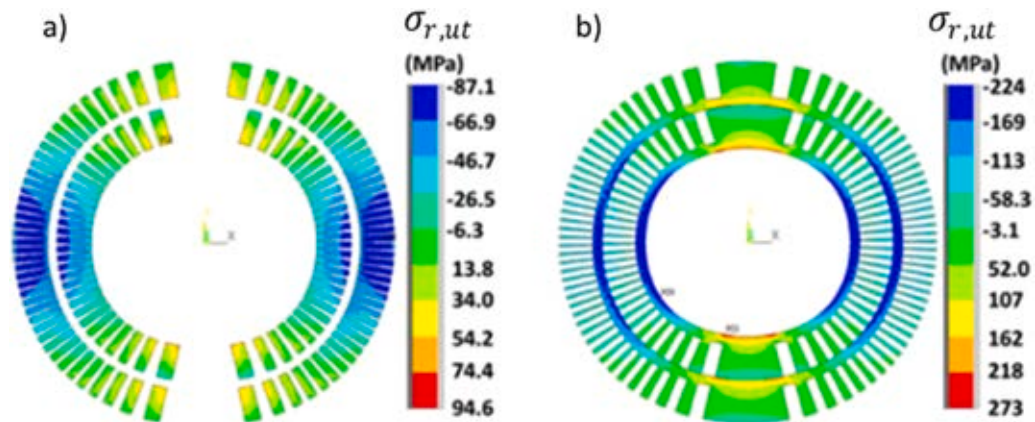


Fig. 5. Azimuthal stress caused by the magnetic operation and cooling-heating cycle: (a) stress on the impregnated cables and (b) stress on the winding former.

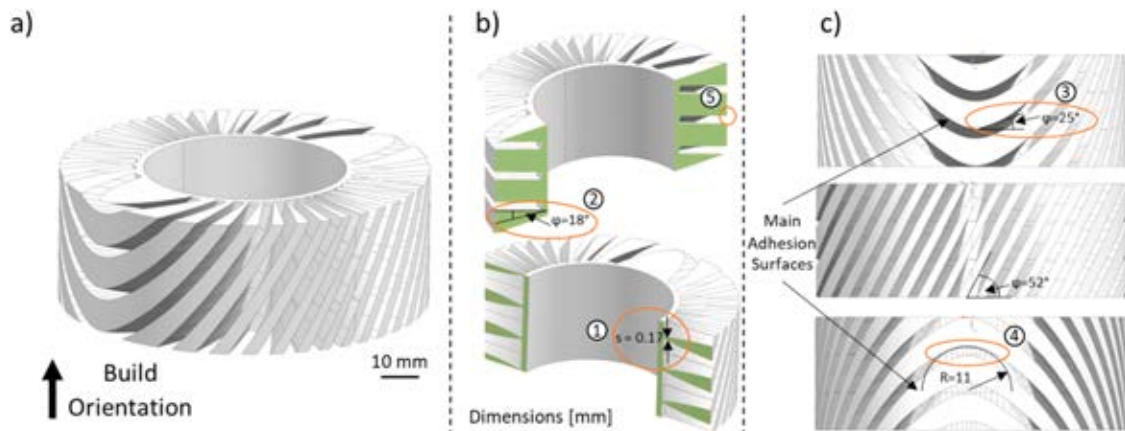


Fig. 6. Ideal winding former with critical design elements 1-5: (a) overall view, (b) cut section views, and (c) side views.

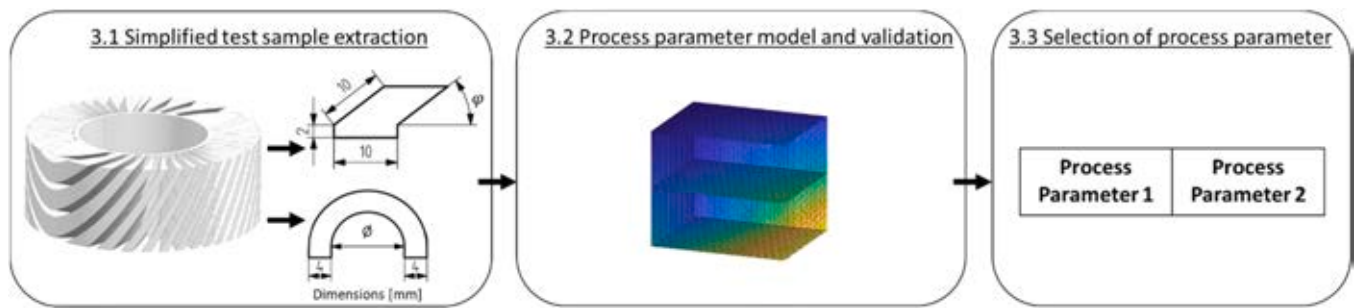


Fig. 7. Development of the process parameter model.

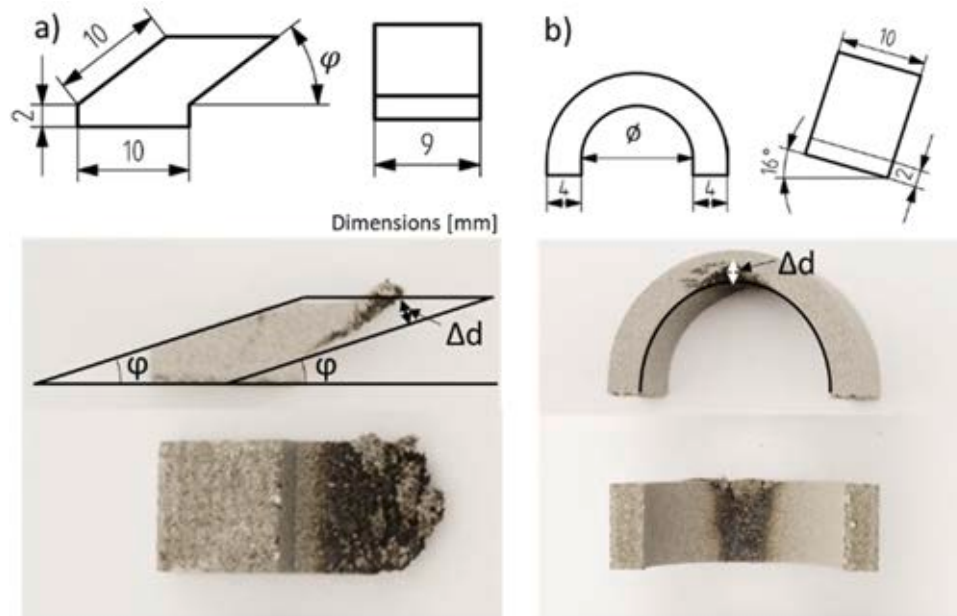


Fig. 8. Form deviation test samples for measuring the form deviation and roughness: (a) overhang and (b) semicircular.

optimized the L-PBF parameters for overhangs and channels of theoretical test parts [19–23]. Wang et al. [19] recommended optimizing parameters according to the overhang angle to avoid local defects and to reduce the form deviation and surface roughness. They developed parameter sets for different overhang angles and argued that the core-shell approach can improve the process efficiency, where different process parameters are used for the core (i.e., inner scan vectors of a layer) and shell (i.e., outer scan vectors of a layer) [16–18]. Cloots et al. [25] recommended that the shell should have a thickness of several millimeters at build angles below 30°, especially for the down-skin layers.

Another promising approach, presented by Rosen et. al. [26] is to assign different process parameter sets to different regions of a part to meet local requirements, named manufacturing elements (MEs) [26]. The ME approach can be used to fabricate critical overhangs in certain elements with a low ρ_{rel}^* for a low form deviation as well as other elements with a high ρ_{rel}^* (e.g., for increased mechanical strength). Rosen et. al. [27] assigned parameters for different MEs of simplified test samples. Xiong et al. [28] further developed the method and applied the fused deposition model (FDM) process to fabricate polymer lattice structures. The ME approach is beneficial for the design, fabrication, and quality of a part. It reduces the form deviation and surface roughness, and it avoids supports at part surfaces with critical overhangs. By assigning locally optimized process parameters, defect-free design elements can be fabricated with the minimum required support. Critical overhangs can be manufactured on internal or inaccessible areas

without supports. Support-free manufacturing can facilitate the texturing of up and down-skin surfaces to improve the mechanical strength of metal composites [29–32]. However, the ME approach has not yet seen wide industrial application, so there is a lack of real-world case studies demonstrating its potential and challenges especially for the L-PBF process. So far, the ME approach has only been applied to simplified test samples and theoretical models. Very few prior works and case studies have examined and validated the application of the ME approach to industrial parts.

This study aims to apply the ME approach to fabricate a complex-shaped 3D part using L-PBF to highlight its advantages and discuss its challenges. A winding former was selected as an example of a real-world application. The end-to-end implementation of the ME approach focused on three major aspects: (1) developing a process parameter model as a basis for optimizing process parameters; (2) segmenting a part into MEs, assigning different parameters, and demonstrating proof of manufacturability on the winding former segment; (3) leveraging the enhanced design freedom for surface texturing to improve the adhesion behavior between the winding former and the cables.

Fig. 3 shows an overview of the work. Section 2 provides background information on the application example and explains the requirements of the part and the necessity of the ME approach. Sections 3–5 present the methods and results for each of the three major aspects. Section 6 discusses the potential and challenges of applying the ME approach to the example part, as well as possible enhancements and research directions. Section 7 summarizes the main results of the work and

$\varphi = 20^\circ$									
$\varphi = 37.5^\circ$									
$\varphi = 55^\circ$									
$\varphi = 72.5^\circ$									
Sample No.	1	2	3	4	5	6	7	8	9
$E_{vd} [J/mm^3]$	11.0	17.9	18.3	26.7	29.8	30.8	50.0	51.3	83.3
$P [W]$	60	60	100	80	100	60	60	100	100
$v [mm/s]$	1400	1400	1400	950	1400	500	500	500	500
$h [mm]$	0.13	0.08	0.13	0.105	0.08	0.13	0.08	0.13	0.08

Fig. 9. Results of the overhang test samples with different process parameters.

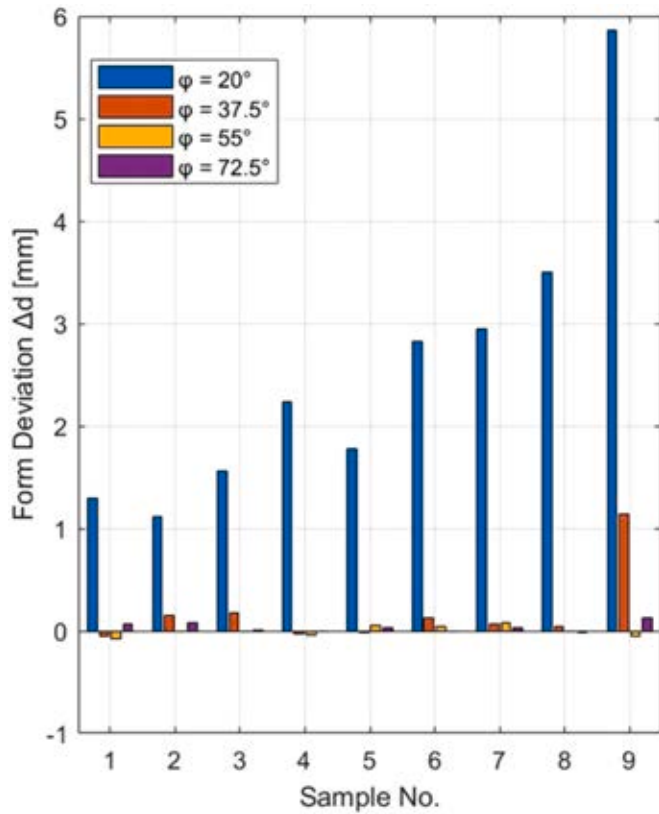


Fig. 10. Form deviations of the overhang test samples with different angles and parameter sets.

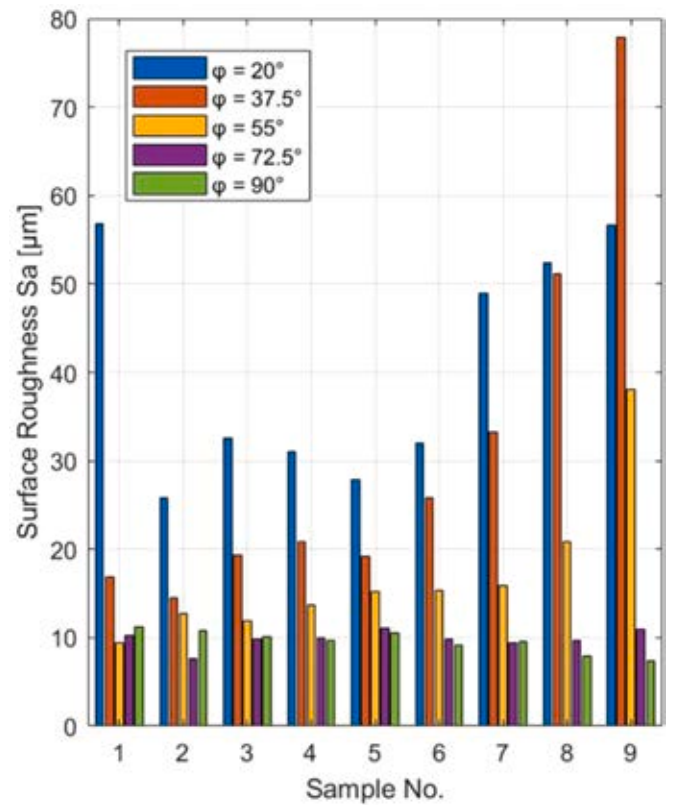


Fig. 11. Down-skin surface roughness of the overhang test samples for different angles and parameter sets.

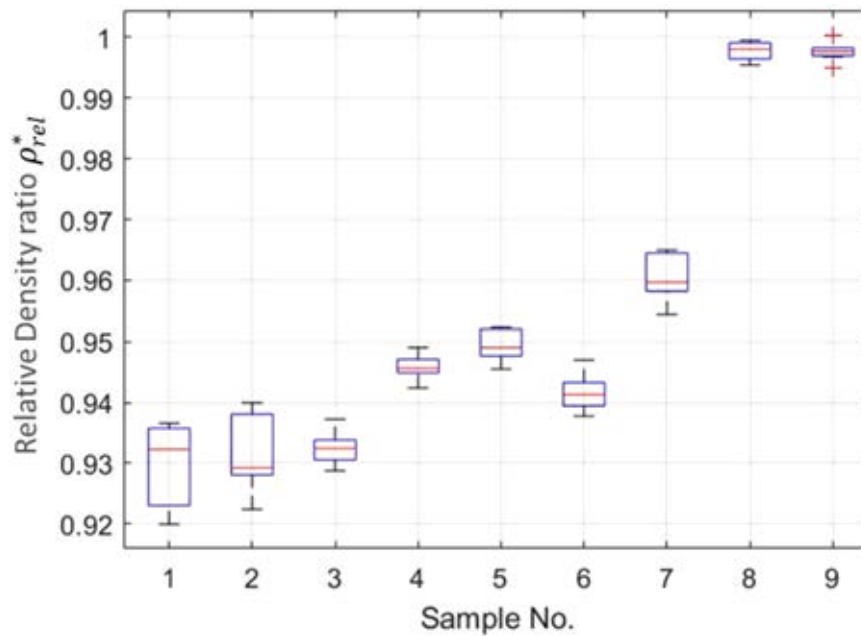


Fig. 12. Relative density ρ_{rel}^* with different parameter sets.

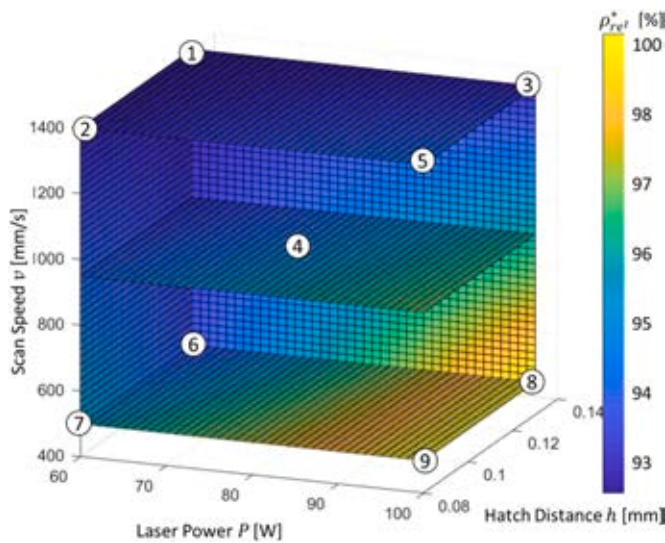


Fig. 13. Graph of the relative density ρ_{rel}^* against the process parameters.

concludes the paper.

2. Background on application

A winding former was selected as the real-world application case study. This is a key component for a special type of superconducting accelerator magnet called the canted cosine theta (CCT) coil, which is used as a bending magnet in a particle accelerator to guide charged particles, such as protons around a curved path. The coil consists of two layers of oppositely tilted solenoidal windings that create two solenoidal fields and generate a pure dipole field. To accelerate charged particles, rectangular cables are wound in the channels of the winding former. After the cables are laid, they are subsequently heat-treated and impregnated with an epoxy resin that bonds them into the channels. Fig. 4 shows the windings and winding former of the coil. During operation, the integrated ribs hold Lorentz forces that act on the turns of wires [33,34]. The shown configuration is used for magnets made from

the Nb₃Sn low-temperature superconductor and generates a high magnetic field of $B = 10$ T with the two opposite tilted helical windings [10, 35]. It was developed for the Future Circular Collider (FCC) program of the European Organization for Nuclear Research (CERN) [10].

The winding former must fulfill three major requirements. The first requirement concerns the load-carrying capacity, which is especially important during the operation of the coil. The critical induced stress for the winding former structure is the azimuthal stress distribution (i.e., radial stress). Fig. 5 shows the simulated azimuthal stress in ANSYS R17.0 given a magnetic induction of $B = 10$ T at a temperature of $T = 1.9$ K. The simulated azimuthal stress at the ultimate tensile stress ranged from $\sigma_{r,ult} = -224$ MPa to $\sigma_{r,ult} = 273$ MPa. The most critical stresses were located at the spars. The second important requirement is the low form deviation of the rib surfaces for sufficient adhesion between the ribs and cables. Adhesion is achieved by using metal–resin joints. Fig. 6 provides the details of their geometry and critical dimensions: (1) a thin ($s = 0.17$ mm thick) rib intersection with high stresses, (2) critical overhang of a concave arc with $\phi = 18^\circ$, (3) critical overhang of a concave arc with $\phi = 25^\circ$, (4) convex arc with a large critical radius and down-skin surface with a width of ~ 11 mm, and (5) down-facing convex arc edge with a radius of $r = 11$ mm. The third requirement is the transfer of the stresses from the cable to the metal ribs through the resin without debonding or increased deformation. This is important to avoid stick-slip motions that can heat the superconductor. To enhance the mechanical strength of the joint, the rib surfaces should be textured to increase the shear strength of the metal–resin joint [36].

Given the requirements and highly complex geometry of the part, its fabrication is very challenging with conventional production technologies, such as milling and casting. Because of their increased costs and technological limitations, these manufacturing technologies were deemed inapplicable [10,37]. Therefore, it was decided to use L-PBF and stainless steel to fabricate the part. However, using standard process parameters with L-PBF leads to droplet formation at the down-skin surfaces of the critical overhang of the ribs, as shown in Fig. 1. Because the geometry of the winding former is predefined, only minor modifications can be applied to the ribs. Additional support structures cannot be used because of the low accessibility of elements with critical overhangs. Such structures would also restrict surface texturing to be applied to the down-skin surfaces. This problem remains even if the orientation of the part is changed. Therefore, the given 3D part geometry cannot be

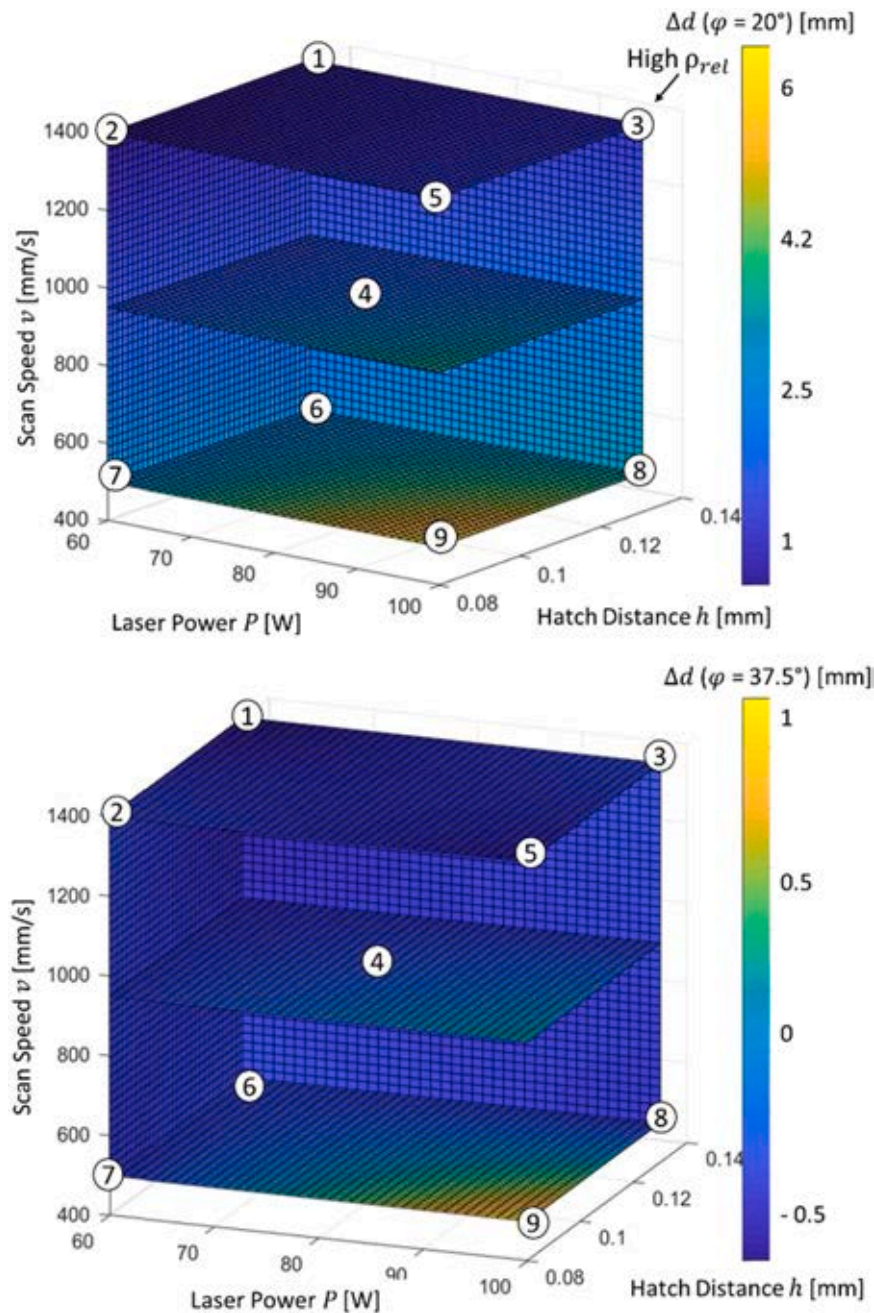


Fig. 14. Graph of the form deviation Δd against the process parameters for overhang test samples: $\varphi = 20^\circ$ (top) and $\varphi = 37.5^\circ$ (bottom).

fabricated by L-PBF without defects, using the standard process parameters and following the standard design rules. Consequently, the process parameters require modification and the ME approach implementation to fabricate the part with a low form deviation without additional supports and to facilitate surface texturing of the down-skin surfaces.

3. Process parameter model

Process parameter model serves as a basis for defining and tailoring a set of process parameters to meet the requirements of a specific element. Fig. 7 shows the development of the model.

3.1. Simplified test sample extraction

Test samples were selected to represent simplified standard test ge-

ometries. All L-PBF test samples and parts were produced with the Mlab Cusing R (GE Additive) machine using stainless steel 316 L and a rubber coater. A Yb:YAG fiber laser was used with a wavelength of 1070 nm, focal diameter of 50 μm , layer thickness t_l of 30 μm , and maximum laser power of 100 W. Test samples were fabricated with different inclination angle φ and diameters \varnothing for different process parameters. The samples were evaluated regarding their surface roughness, form deviation, and material density. The form deviation of the overhang samples was analyzed optically using Fiji software. Fig. 8 shows the geometric parameters and measured form deviation Δd between the CAD part and the L-PBF Part. The image of the test pieces was captured by a NIKON D5200. The pixel size was referenced by a 0.01 mm microscope calibration ruler slide. Then a clear contrast line between the background and the L-PBF part was used to place the ideal circles, lines, and actual part contours within Fiji. The ideal shape was derived from the CAD data. The precise position of the ideal shape and the L-PBF





























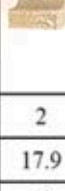
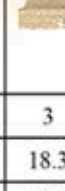





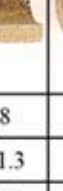
$\varnothing = 23 \text{ mm}$									
$\varnothing = 18 \text{ mm}$									
$\varnothing = 13 \text{ mm}$									
$\varnothing = 8 \text{ mm}$									
Sample No.	1	2	3	4	5	6	7	8	9
$E_{vd} [\text{J}/\text{mm}^3]$	11.0	17.9	18.3	26.7	29.8	30.8	50.0	51.3	83.3
$P [\text{W}]$	60	60	100	80	100	60	60	100	100
$v [\text{mm}/\text{s}]$	1400	1400	1400	950	1400	500	500	500	500
$h [\text{mm}]$	0.13	0.08	0.13	0.105	0.08	0.13	0.08	0.13	0.08

Fig. 15. Results of the semicircular test samples with different process parameters.

contours was set by the user. In a further step, the maximum distance between the ideal lines and the corresponding contrast lines of the overhanging surfaces of the L-PBF part was measured. Based on this measurement, the shape deviation between the ideal shape and the actual shape of the test specimens was analyzed.

3.2. Process parameter model and validation

For the development of the process parameter model, a full factorial design of experiments was applied with one central point (four replications) and eight cube points for the form deviation test samples. The factors were laser power ($P = 60, 80, \text{ and } 100 \text{ W}$), scan speed ($v = 500, 950, \text{ and } 1400 \text{ mm/s}$), and hatch distance ($h = 0.08, 0.105, \text{ and } 0.13 \text{ mm}$). These yielded a volumetric energy density range of $E_{vd} = 11\text{--}83.3 \text{ J}/\text{mm}^3$. The volumetric energy density E_{vd} is calculated as: $E_{vd} = \frac{P}{v \cdot h \cdot t_l}$. The parameters P , v , and h are important because they affect the form deviation Δd and relative density ρ_{rel}^* [19]. The layer thickness t_l is kept constant. For each cube point and for each geometry, one sample was fabricated. Because of possible measurement inaccuracies, four samples were produced at the central point to ensure a stable statistical model. This design of experiment was applied to different geometric parameters.

Overhang test samples were built with four angles: $\varphi = 20^\circ, 37.5^\circ, 55^\circ, \text{ and } 72.5^\circ$. Fig. 9 shows the samples fabricated for different process parameters. The dross formation, partly molten particles, and the amount of discoloration increased with E_{vd} and with decreased angle φ .

The form deviation Δd of the test samples is shown in Fig. 10. Significant form deviations were observed at $\varphi = 20^\circ$ for Nos. 1–9 and at

$\varphi = 37.5^\circ$ for No. 9. At $\varphi = 20^\circ$, No. 2 had the minimum form parameter set with $\Delta d = 1.1 \text{ mm}$; here, dross formation was already visible. At $\varphi = 37.5^\circ$, No. 8 was usable with $\Delta d = 0.04 \text{ mm}$; here, the amount of discoloration was already visible, but there was no strong form deviation.

The mean roughness S_a was measured as per ISO 4287 by using Keyence VK-X200K confocal 3D laser microscope with a z-direction resolution of 0.5 nm and a Gaussian low pass filter of $5 \mu\text{m}$ with a corresponding 3×3 pixel matrix. A surface shape correction was carried out for all measurement data to obtain comparable plane measurement results. Fig. 11 shows the results for the down-skin surface roughness S_a . Except for No. 1, the roughness increased with E_{vd} . For No. 1, the relative density ρ_{rel}^* resulted in a porous structure on the down-skin surface. Therefore, the roughness is higher for this sample. Additionally, S_a tends to increase with decreasing φ .

Fig. 12 plots the relative densities with different parameter sets; ρ_{rel}^* increased with E_{vd} . The maximum value of ρ_{rel}^* was 0.998 at Nos. 8 and 9. The lowest ρ_{rel}^* value was 0.930 at Nos. 1–3.

A linear regression model was used to visualize the relative density ρ_{rel}^* and form deviation Δd at $\varphi = 20^\circ$ and $\varphi = 37.5^\circ$. The numbers in the graphs in Figs. 13 and 14 represent the sample number and their position in the model. Fig. 13 visualizes the relative density for the factors.

The critical angles are $\varphi = 20^\circ$ and $\varphi = 37.5^\circ$, shown in Fig. 10. Therefore, these two angles were used to generate a parameter model for the form deviation, visualized in Fig. 14.

Next, the results for the semicircular test samples were analyzed to compare results and validate the overhang test samples. Fig. 15 shows the results of the semicircular test samples with different process

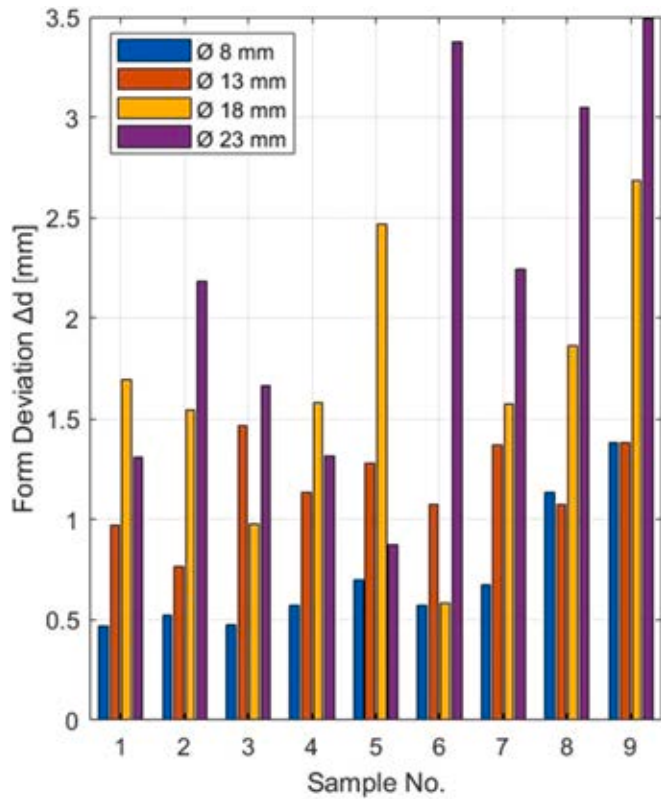


Fig. 16. Form deviations of the semicircular test samples with different diameters and parameter sets.

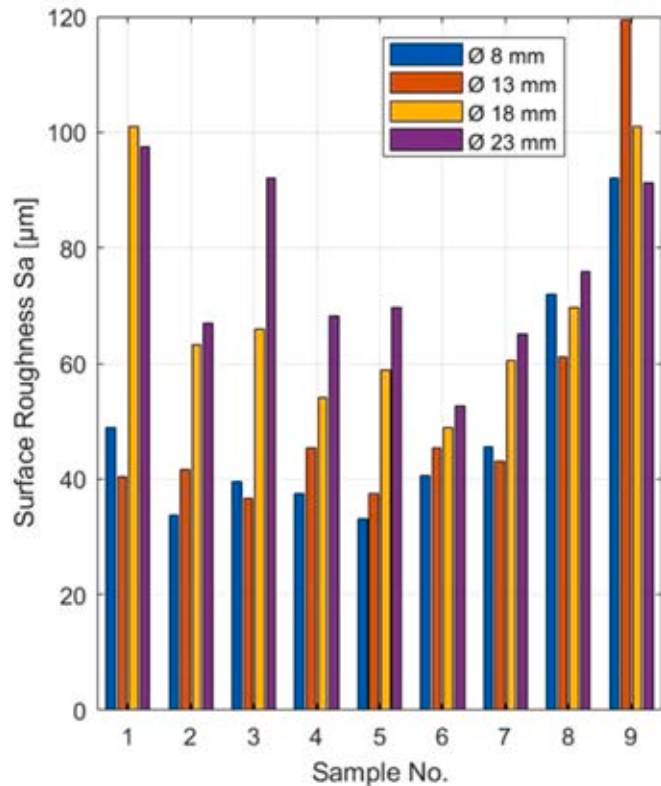


Fig. 17. Down-skin surface roughness results of the semicircular test samples.

parameter sets and diameters. The dross formation increased with an increase in the energy E_{vd} and diameter, which is indicated by the partly molten particles and increased amount of discoloration of the samples. Fig. 16 shows the form deviations Δd of the semicircular test samples. A maximum diameter of $\varnothing = 23$ mm was manufactured with relatively low dross formation and amount of discoloration at No. 1. Fig. 17 shows the measured down-skin S_a results for the semicircular test samples. The results varied significantly because of the increased dross formation; however, S_a tends to increase with an increase in the diameter and E_{vd} .

3.3. Process parameter selection

The results demonstrated the influence of different process parameters on the density, form deviation, and surface roughness. The different parameter sets indicated the trade-off that either ρ_{rel}^* could be maximized, or Δd can be minimized. The most suitable parameter sets for low and high ρ_{rel}^* belonged to Nos. 2 and 8, respectively; these are summarized in Table 1.

4. Manufacturing elements

The part was segmented into MEs that were assigned with process parameters taken from the model presented in Section 3. Fig. 18 shows the ME approach.

4.1. Segmentation of part into different MEs and parameter assignment

Fig. 19 shows the ideal design of the winding former and the critical design elements 1–5. To ensure the functional performance of the part, the critical elements need to be manufactured as precisely as possible. The part orientation has a strong influence on the quality. The figure shows the final part design and orientation of the winding former including the MEs, which are shown in green (high ρ_{rel}^*) and blue (low ρ_{rel}^*). The critical design elements are indicated with the orange circles and numbers 1–5. The entire winding former had an overhang with $\varphi = 73^\circ$. The winding former was rotated so that the coater was oriented 15° to the critical convex overhang. Table 2 summarizes the critical design elements and measures for improvement.

4.2. Proof of manufacturability

The manufacturability of the critical MEs was demonstrated by the winding former. The steep convex overhang (ME No. 2 in Table 2) was 10 mm longer than that of the overhang test samples. To determine the minimum inclination without dross formation, a series of concave ribs with five angles ranging between $\varphi = 30^\circ$ and 40° was tested. The minimum possible angle was $\varphi = 35^\circ$, which was 17° more than that of the original test sample ($\varphi = 18^\circ$). To manufacture a design without excessive discoloration and dross formation, the angle of the convex arc was used to define the orientation of the entire winding former. The orientation of the winding former was varied from $\varphi = 90^\circ$ to $\varphi = 73^\circ$ (see Fig. 19). Fig. 20 shows the L-PBF process including the Keyence 3D laser microscopy images in which porous regions are visible. Fig. 21 shows the final printed winding former. The final surface roughness was slightly less than that of the process parameter model but was sufficiently close to the approximation. Then the fabricated part in Fig. 22 was scanned compared to the CAD geometry. For the scan, the GOM ATOS Core 200 3D scanner was used. The 3D measurement system is based on the optical stereo camera principle. A global best-fit algorithm minimizes all deviation between the CAD surface and the measured surfaces. The deviation is based on the surface normal between the CAD part and the measured part. The calibration object was a sphere artifact and measured on a numerically corrected and calibrated coordinate measuring machine of type PRISMO navigator (Serial No. 156544) by Carl Zeiss. According to the acceptance report (VDI/VDE 2634, Part 3) of

Table 1
Selected process parameters.

	Sample No.	P [W]	v [mm/s]	h [mm]	E_{vd} [J/mm ³]	ρ_{rel}^*	Min. φ [°]	Δd [mm]
Low ρ_{rel}^*	2	60	1400	0.13	17.83	0.931	20	1.11
High ρ_{rel}^*	8	100	500	0.08	51.28	0.998	37.5	0.15

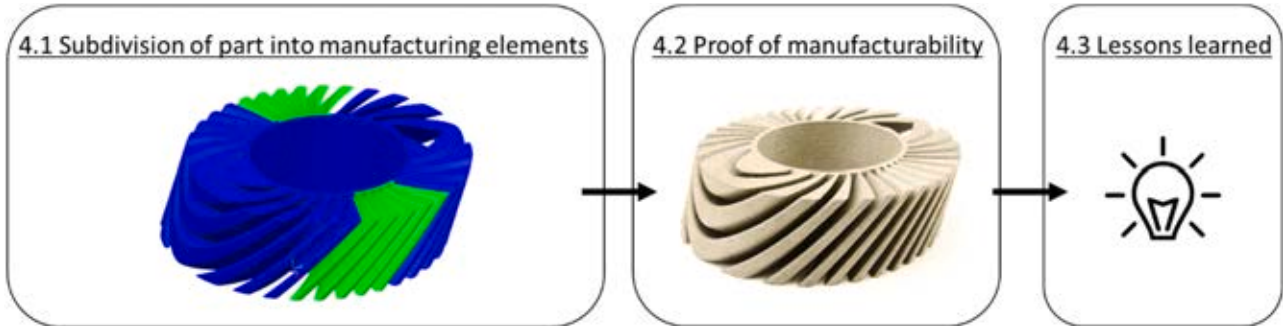


Fig. 18. ME approach.

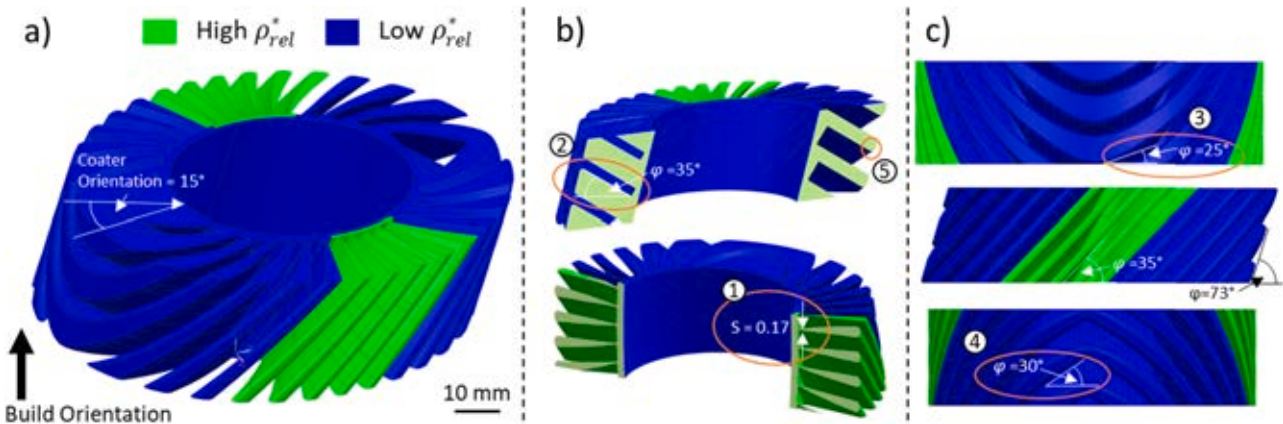


Fig. 19. Design of the winding former optimized for L-PBF including the critical design elements 1–5: (a) overall view, (b) cut section views, and (c) side views. (For interpretation of the references to colour in this figure, the reader is referred to the web version of this article.)

the calibration certificate, is the length measurement error 0.014 mm, of the GOM system, for a nominal length of 134.999 mm.

The critical design elements showed a form deviation $\Delta d = -0.37$ mm for the ribs at the outer position and at the intersection. The concave arc had a maximum form deviation of $\Delta d = +0.29$ mm at the down-skin surface. The convex overhang had a maximum form deviation of $\Delta d = -0.41$ mm at the down-skin surface and $\Delta d = +0.26$ mm at the up-skin surface. The maximum form deviation was $\Delta d = +0.42$ mm in the positive direction and $\Delta d = -0.41$ mm in the negative direction. The large form deviation on the lower side of the rib may have been caused by the removal process, which used a band saw. Except for the lower side of the ribs, the form deviations arise from the L-PBF process. The maximum negative form deviation of $\Delta d = -0.41$ is caused by the L-PBF process inaccuracies of the extreme geometrical convex down-skin surface. For the final application of the winding former, the resin can compensate the measured deviations for an ideal alignment of the cables.

4.3. Lessons learned

The following lessons were drawn from the manufacturing of the winding former. First, a sharp intersection between different MEs is critical in the case of mechanical stress and may act as a predefined

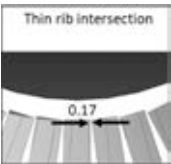
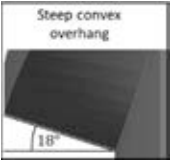
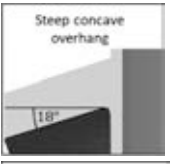
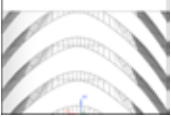
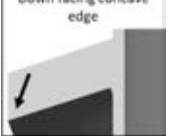
notch, shown in Fig. 23. To guarantee strong bonding between the ribs and spar, the area of the intersection with high ρ_{rel}^* should be increased. In the case of high mechanical stress, the boundary of the ME has to be carefully chosen to match positions with low mechanical stress. With regard to the density of a single ME, the mechanical properties can be taken from the literature [38]. Second, the part orientation needs to be defined as soon as the critical design elements are determined [39]. Different elements should be prioritized according to their importance. The minimum orientation angle of a critical element should be defined, and lower-priority elements should be redesigned (e.g., with a droplet shape) if possible. Finally, different elements should be prioritized according to the coater direction. The coater direction with respect to the critical overhang has a large influence on the manufacturing quality [15]. The down-skin surfaces should be facing away from the coater for improved quality [25].

5. Surface texturing

The design freedom from the reduced need for support structures can be utilized for surface texturing. The process parameters and MEs described in Sections 3 and 4 were applied to enable surface texturing. The surface texture has the shape of dimples to increase the adhesion bonding between the metal surface and epoxy. The effect of the surface

Table 2

Critical design elements with requirements, comments, design measures, and process parameters.

No.	Requirements	Comment	Design measure	Process Parameter
1	 Thin rib intersection 0.17	The rib intersection is extremely thin and needs to be manufactured with parameters that maximize the tensile strength to avoid bending deformation and ripping during the assembly process. The form deviation for the down-skin surfaces of concave ribs should be minimized. However, the stiffness needs to be maximized at this position.	–	High ρ_{rel}^*
2	 Steep convex overhang 18°	The convex arc is critical, and no form deviation is allowed because this surface is important for guiding the cable. This is especially challenging given the overhang angle of $\varphi = 25^\circ$ (No. 3 in Fig. 19) because this design is fixed.	Reorient the entire winding former and overhang	Low ρ_{rel}^*
3	 Steep concave overhang 18°	The concave down-facing overhang has an angle of $\varphi = 18^\circ$.	Redesign to a droplet shape	Low ρ_{rel}^*
4	 Large concave radius	The down-skin surface has a radius of $r = 11$ mm.	Redesign to a droplet shape	Low ρ_{rel}^*
5	 Down facing concave edge	The edge of the radius is facing down into the powder bed.	Use a 1.5 mm radius to avoid a sharp down-facing edge	Low ρ_{rel}^*

texture was then investigated. Finally, the surface texture shape was transferred to the 3D geometry. Fig. 24 shows the surface texturing approach.

5.1. Test samples

To examine the influence of surface texturing, adhesion samples were fabricated, and a shear test was performed. Stainless Steel 316 L cubes with four different morphologies were bonded together with CTD101K, which is a widely used epoxy resin system for cryogenic applications. Fig. 25 shows the shear test samples, which were manufactured according to the parameter set for high ρ_{rel}^* . The L-PBF flat surface was the native surface after sintering without post-treatment, Fig. 25(a). The L-PBF textured surface had a dimple structure, Fig. 25

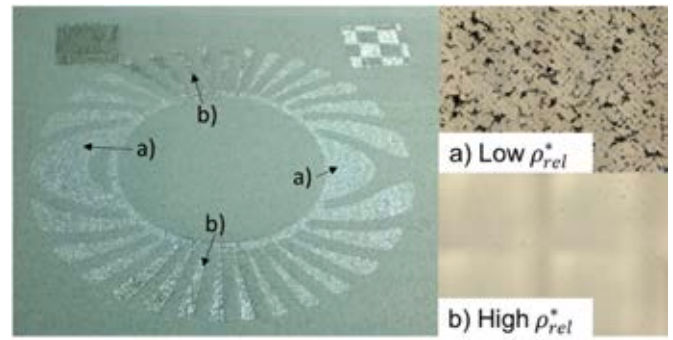


Fig. 20. L-PBF process of the winding former including the grinding sections corresponding to (a) low ρ_{rel}^* and (b) high ρ_{rel}^* .

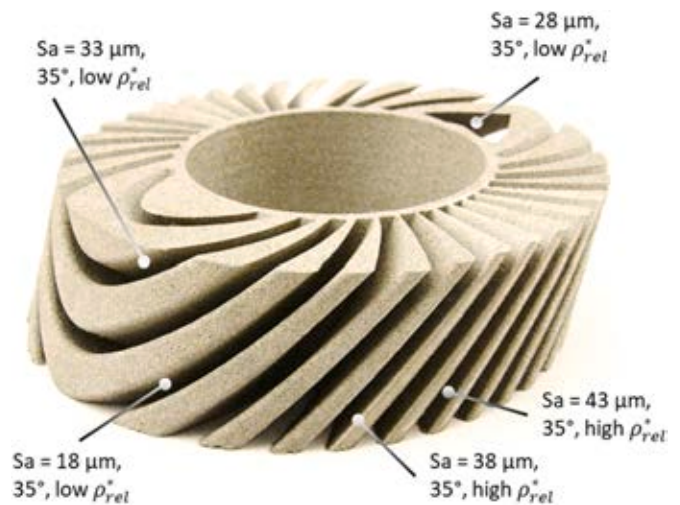


Fig. 21. Final winding former including the measured roughness.

(b). The blank steel surface was from a commercial stainless steel square rod, Fig. 25(c), produced by extrusion. The blank steel corundum-blasted surface, Fig. 25(d), was the same material but blasted with corundum grains that were 600–850 μm in size. The inset in Fig. 25 plots the dimensional geometry of the hemispherical dimples. Fig. 26 plots the measured roughness and shape. The highest roughness was $Sa = 12.2$ μm for the textured surface. The second-highest roughness was observed for the L-PBF flat surface, which was characterized by sintered particles. The blank steel had similar Sa . However, the corundum-blasted surface was more uniform than the blank steel and had a comparable morphology to that of the L-PBF flat surface.

5.2. Shear test results

Shear samples were produced by aligning three cubes of the same kind with a gap of 0.5 mm in the mold. The mold was subsequently filled with CTD-101K, which is a high-performance epoxy resin developed for radiation applications with improved wetting and excellent impregnation of large winding formers with highly tortuous paths, and the samples were then cured at 135 °C for 1.5 h. The shear test was performed on a Zwick Z202 with a 20-kN load cell. Both outer cubes were clamped, and the middle sample was sheared off by pressing a piston on the middle cube, as shown in Fig. 27. Rubber sheets of 2 mm thickness were placed on top and below the rectangular piston to ensure an evenly distributed loading. Three samples were tested for each of the four surfaces. Fig. 28 shows a boxplot of the maximum shear strength. In every case, adhesion failure led to the fracture of the sample. The L-PBF blank surface had the lowest median value of 11.03 MPa. The highest

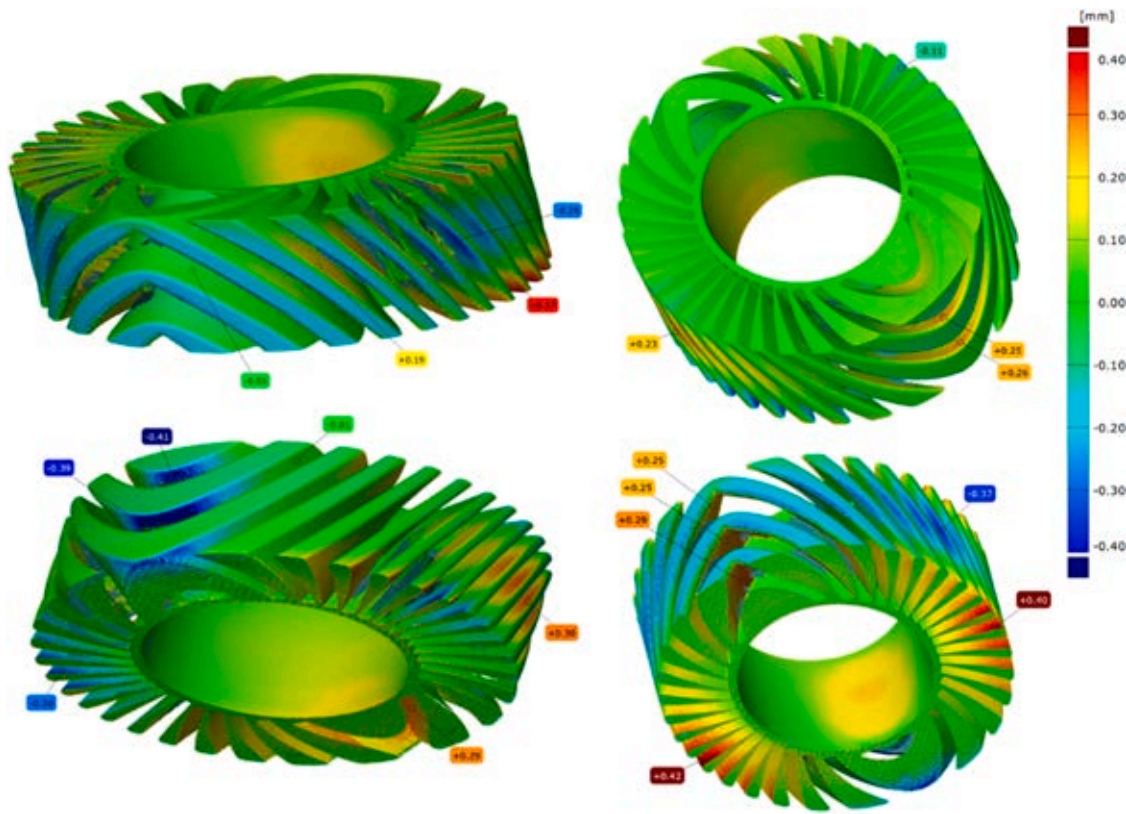


Fig. 22. Comparison of the CAD geometry and measured geometry of the winding former.

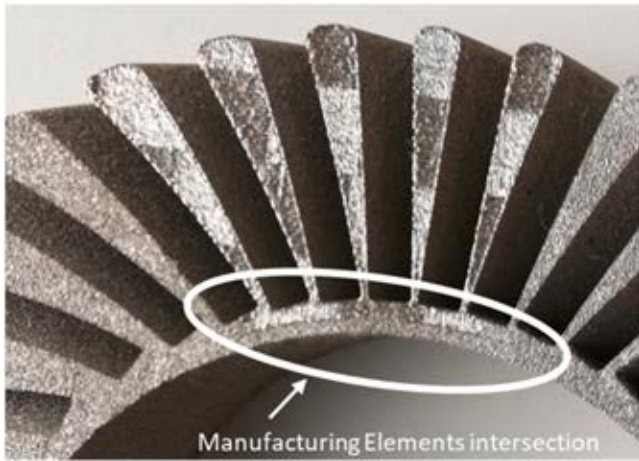


Fig. 23. Thin rib intersection between spare and ribs.

median value of 17.94 MPa was observed for the L-PBF textured surface. Thus, surface texturing significantly increased the maximum shear strength of the L-PBF surface by 63%.

5.3. Transferring textures onto 3D geometry

Fig. 29 shows the manufacturing of ribs that were textured on the down-skin and up-skin surfaces. The ME approach made it possible to texture surfaces even with angles of $\varphi = 28^\circ$. Especially for the convex overhang with $\varphi = 35^\circ$, texturing the surface with dimples is critical to ensuring a stable L-PBF process.

6. Discussion

This section discusses first the opportunities and challenges of the ME approach, visualized in Fig. 30. This follows a discussion of the improved adhesion from surface texturing and possible enhancements in the future.

6.1. Opportunities

Compared to standard process parameters, the use of the ME approach increases the design freedom, avoids the excessive use of sacrificial support structures, and enhances the process capabilities of L-PBF, even for a complex real-world case study.

The low ρ_{rel}^* uses a scan speed of $v = 1400$ mm/s which is 2.8 times faster than using the high ρ_{rel}^* with a scan speed of $v = 500$ mm/s. Using the ME approach increases the scan speed and therefore reduces the L-PBF process time. Depending on the scan area and build height, this can reduce the processing time by hours and thus save manufacturing costs. Applying the ME approach further reduces the need for support structures. This reduces the L-PBF build time as less raw powder has to be melted, which leads to strong cost reductions [8]. Reducing support structures further leads to a reduced support removal effort. Since the removal of support structures is highly time-consuming and manual, labor hours can be saved by using the ME approach. This leads to major cost reductions in post-processing [8].

The case study further demonstrated that the ME approach improves the form deviation and roughness. In addition, the relative density of MEs can be adjusted, which can be used to increase the process speed and therefore reduce the lead time and machining costs.

Further refinement of the MEs into smaller sub-elements would further improve the design freedom, process speed, and material properties. This can be realized by applying a core-shell approach [25].

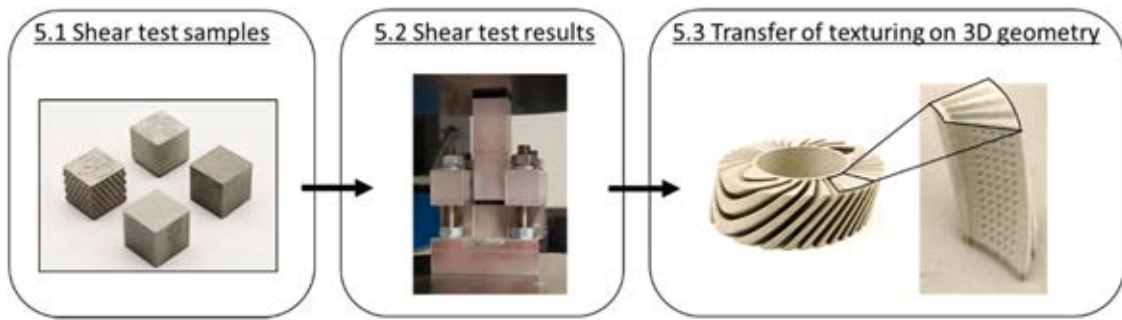


Fig. 24. Surface texturing approach.

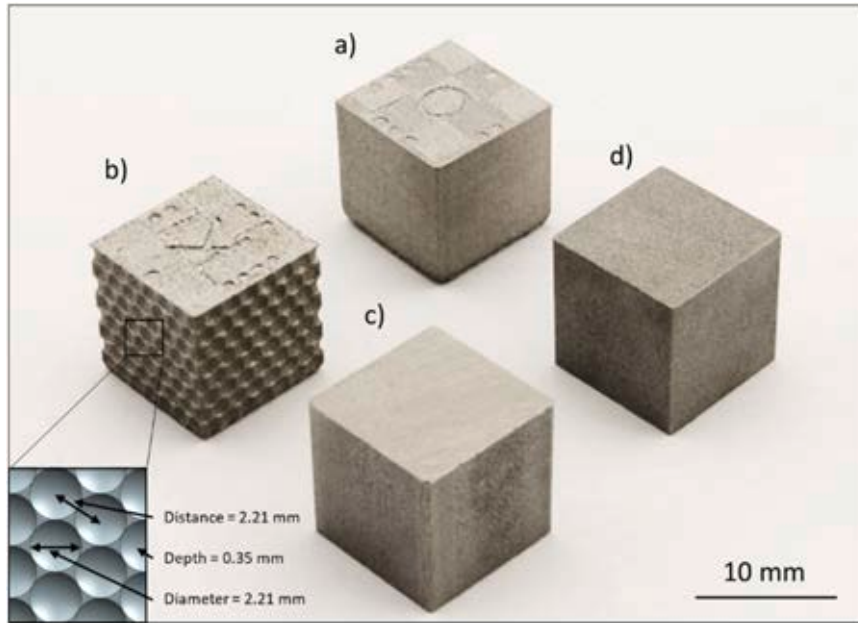


Fig. 25. Shear test samples: (a) L-PBF flat surface, (b) L-PBF textured surface, (c) blank steel, and (d) blank steel corundum-blasted surface. The inset includes the geometric dimensions of the dimpled texture.

6.2. Challenges

Applying the ME approach to AM is currently a time-consuming process because of the use of different software tools and transfers in the data-process chain. Within the CAD software, a part has to be divided into different elements to assign the desired parameter set. In the pre-process and process slicer, the elements are then merged again. This problem should be solved in the next years.

It is difficult to generalize the process parameter model for other geometries. As a validation example, the process parameters from the overhang test samples were transferred to the semicircular test samples. A minimum ϕ of 20° was realized for the test samples, but the case study realized a minimum ϕ of 25° . The length and size of the overhang vary with the part geometry, which can lead to differences between the test samples and parameter model. This can increase the melt pool size, and several test iterations are required to manufacture the part with the desired quality. Additionally, the applicability of surface texturing on complex L-PBF parts is limited. For example, the application on down-facing overhangs with an angle of 25° is critical and should be carefully evaluated depending on the individual geometry. Consequently, A design-specific investigation is required for determining the critical elements and orientation. In situ process monitoring may help solve this problem. Laser tracking strategy is an important factor for ensuring part quality, as reported by Cloots et al. [25].

Further applications of the ME approach requires optimization of the connections between MEs. The material is not homogeneous at the intersections and may act as a predefined notch. This is similar to the challenges faced by hybrid AM for the conventional manufacture of raw materials [40]. Adjusting the melt pool size can improve the connection [41]. More research is required on the connections between MEs.

6.3. Adhesion

In the shear test, the L-PBF textured surface had a significantly higher maximum shear strength of 17.94 MPa, than the other test samples because of the increased adhesion from the dimple structure. Changing the microstructure had no significant influence on the maximum shear strength, as seen for the L-PBF flat surface ($S_a = 6.5 \mu\text{m}$) and blank steel ($S_a = 5.2 \mu\text{m}$), or a minor influence, as seen for the blank steel corundum-blasted surface ($S_a = 5.8 \mu\text{m}$). In the literature, the surface roughness has been found to influence the shear strength [30]. Therefore, in this study, the differences in the surface roughness may have been too small to affect the measured shear strength. Further development of the surface texture at the macroscale may increase the maximum shear stress [42]. Graziosi et al. [36] investigated different 3D geometries for FDM and L-PBF. They showed that 3D structures may improve the shear-junction adhesion strength, which can be used to improve the adhesion between the cable and winding former. Therefore,

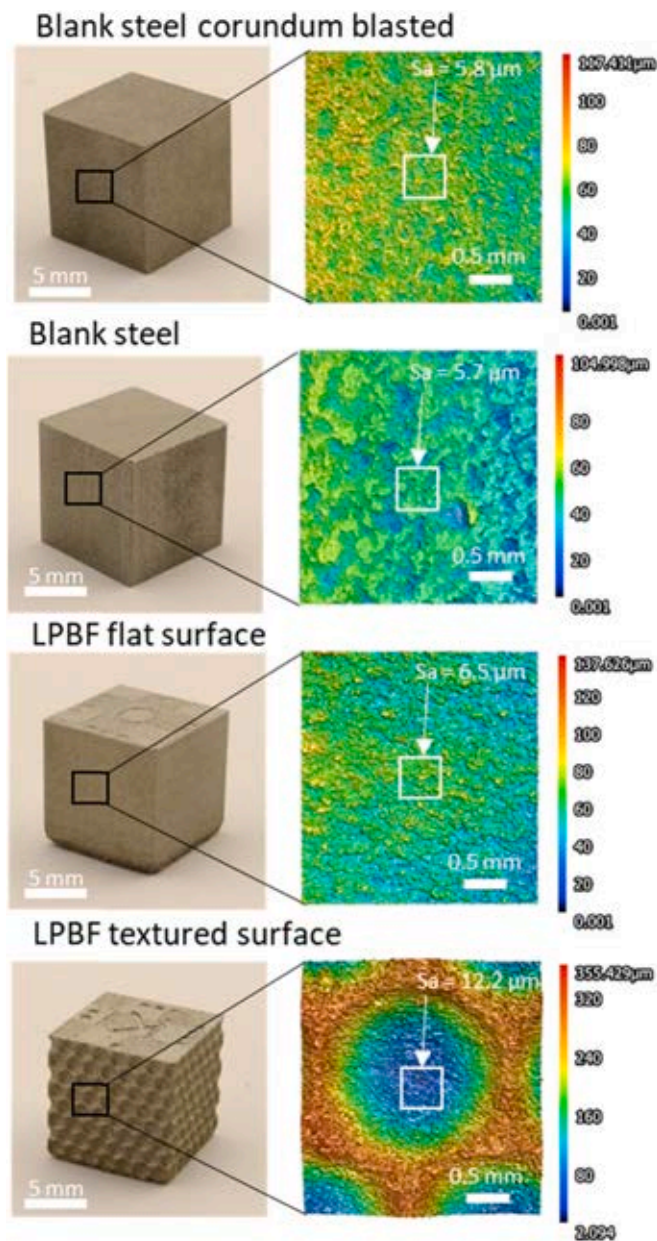


Fig. 26. Shear test samples. Roughness and morphology measurement.

the applicability of 3D geometries (e.g., lattice structures) to winding formers would be interesting to investigate. Subscale adhesion tests in shear, tension, at room temperature, and cryogenic temperatures are required before such structures can be applied to actual winding formers.

In this study, a winding former section was produced with a short length. However, for the final application, a length of several meters or even kilometers is required. To produce this length, a continuous infinite metal AM process should be developed. Another solution could be the production of segments that are connected by material-, force-, or shape-type bonds.

6.4. Enhancements

A continuous digital workflow is fundamental for further developments of the ME approach to reduce the process time and simplify the process.

To improve the design process, an algorithm should be developed for

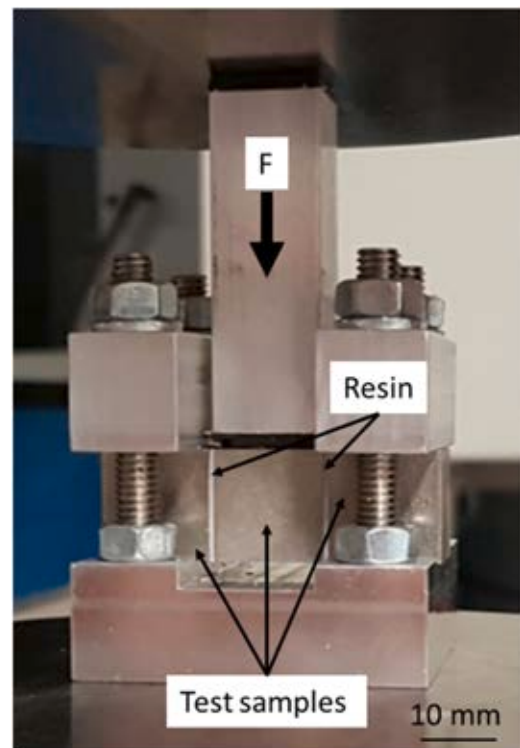


Fig. 27. Shear test setup.

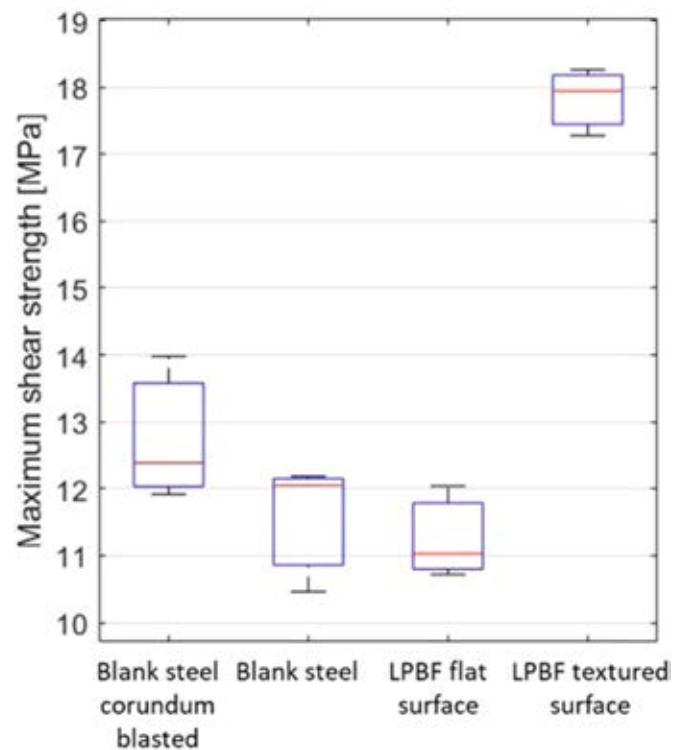


Fig. 28. Maximum stresses for the different shear test samples.

automatic division of a part into functional MEs based on the geometric and functional boundaries. In addition, the assignment of standardized parameter profiles to elements should be automated.

The core-shell approach should be implemented to further increase the efficiency of the ME approach. Further refinement of the MEs could

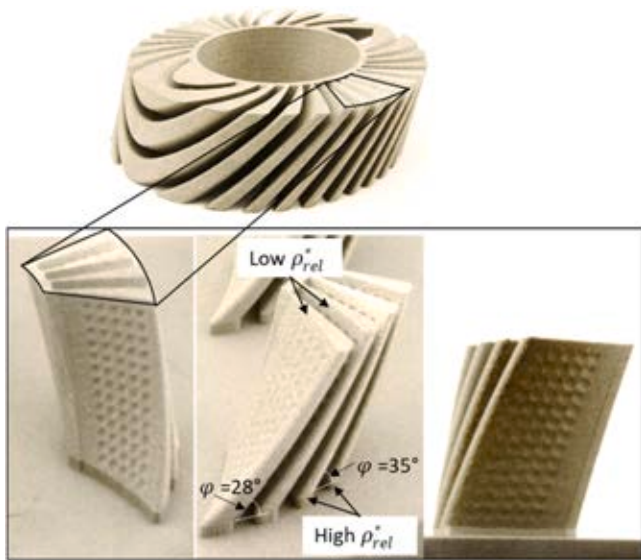


Fig. 29. Demonstration of the surface texturing on the winding former ribs.

lead to functionally graded materials. However, this requires an improved digital workflow for further practical applications.

In situ monitoring of aspects such as the melt pool would further simplify the ME approach and allow the process parameters to be optimized to realize the desired properties of an ME [41].

Following design for AM guidelines, such as those specified by Adam and Zimmer [14], could improve design understanding for MEs to maintain the ideal shape of a part.

The results of this study proved that the ME approach could be applied to manufacture the winding former. This type of coil can be used to realize proton beams for accurately treating cancerous tumors [43]. Currently, only a small number of patients have access to this treatment because the machines are very expensive and limited to a small number of hospital centers, such as Heidelberg, Germany or the Paul Scherer Institute, Switzerland [33]. Introducing superconducting coils would drastically reduce the footprint required for proton beam therapy and thus facilitate its application to many more hospitals. A particular advantage of CCT magnets in this context is that if the winding former is bent, a bent magnet can be wound without additional complications caused by the bending radius. This coil type is also applicable to the CERN's FCC program [10].

7. Conclusions

Low geometrical tolerances, high-quality material properties, and low surface roughness are challenges in AM. To increase the process capabilities, a promising concept is to tailor process parameters for the fabrication of a part. Instead of selecting identical process parameters to the geometry of the whole part, different sets of process parameters are assigned to different regions, called manufacturing elements (MEs). This paper presents an end-to-end implementation of the ME approach to a winding former. Three main advantages of the ME approach were identified: Significant reduction of required sacrificial support structures based on the reduced build angles and less post-processing efforts; reduced AM processing time due to less sacrificial support structures and a higher laser speed; and local adjustment of the material and surface properties. The ME approach facilitated support-free fabrication of the winding former with build angles of as low as 25°. The enhanced design freedom enabled surface texturing, which allowed the maximum shear strength to be improved by 63% compared to that of a nontextured surface. Future research should focus on the development of a continuous digital workflow of the ME approach, an automated part segmentation process, the implementation of the core-shell approach, and in situ monitoring to realize the direct adjustment of the process parameters.

Funding

This work was supported by the Swiss State Secretariat for Education, Research and Innovation SERI.

CRediT authorship contribution statement

Julian Ferchow: Conceptualization, Methodology, Validation, Formal analysis, Investigation, Manufacturing, Writing – original draft, Visualization. **Manuel Biedermann:** Conceptualization, Methodology, Writing – review & editing. **Pascal Müller:** Process Parameter Model, Validation, Analysis, Case Study, Design Surface Texturing, Manufacturing, Writing – review & editing. **Bernhard Auchmann:** Supervision, Writing – review & editing. **André Brem:** Shear test, Writing – review & editing. **Mirko Meboldt:** Supervision, Writing – review & editing.

Declaration of Competing Interest

The authors declare that they have no known competing financial

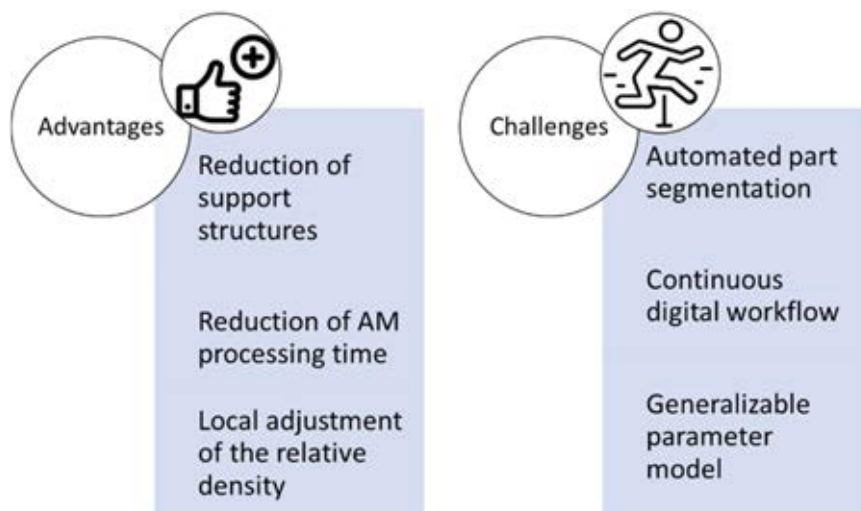


Fig. 30. Identified main advantages and challenges of the ME approach.

interests or personal relationships that could have appeared to influence the work reported in this paper.

References

- [1] Wohlers Report, Wohlers Associates, Fort Collins, (2020).
- [2] R. Leal, F.M. Barreiros, L. Alves, F. Romeiro, J.C. Vasco, M. Santos, C. Marto, Additive manufacturing tooling for the automotive industry, *Int. J. Adv. Manuf. Technol.* 92 (2017) 1671–1676, <https://doi.org/10.1007/s00170-017-0239-8>.
- [3] D. Deradjat, T. Minshall, Implementation of rapid manufacturing for mass customisation, *J. Manuf. Technol. Manag.* 28 (2017) 95–121, <https://doi.org/10.1108/JMTM-01-2016-0007>.
- [4] S. Raikar, M. Heilig, A. Mamidanna, O.J. Hildreth, Self-terminating etching process for automated support removal and surface finishing of additively manufactured Ti-6Al-4 V dissolvable Ti64 supports process flow, *Addit. Manuf.* (2020), 101694, <https://doi.org/10.1016/j.addma.2020.101694>.
- [5] S. Nelaturi, M. Behandish, A.M. Mirzendehtdel, J. de Kleer, Automatic support removal for additive manufacturing post processing, *CAD Comput. Aided Des.* 115 (2019) 135–146, <https://doi.org/10.1016/j.cad.2019.05.030>.
- [6] K. Cooper, P. Steele, B. Cheng, K. Chou, Contact-free support structures for part overhangs in powder-bed metal additive manufacturing, *Invent. MDPI* 3 (2018) 1–11, <https://doi.org/10.3390/inventions3010002>.
- [7] F. Ceccanti, A. Giorgetti, P. Citti, A support structure design strategy for laser powder bed fused parts, *Procedia Struct. Integr.* 24 (2019) 667–679, <https://doi.org/10.1016/j.prostr.2020.02.059>.
- [8] J. Jiang, X. Xu, J. Stringer, Support structures for additive manufacturing: a review, *J. Manuf. Mater. Process.* 2 (2018) 1–23, <https://doi.org/10.3390/jmmp2040064>.
- [9] H.S. Carslaw, J.C. Jaeger, *Conduction of Heat in Solids*, Clarendon press, 1992.
- [10] G. Montenero, B. Auchmann, L. Brouwer, C. Calzolaio, S. Caspi, G. Rolando, S. Sanfilippo, Mechanical structure for the PSI Canted-Cosine-Theta (CCT) magnet program, *IEEE Trans. Appl. Supercond.* 28 (2018) 1–5, <https://doi.org/10.1109/TASC.2017.2787596>.
- [11] A.K. Lianos, S. Koutsoukos, H. Bikas, P. Stavropoulos, Manufacturability assessment and design for AM, *Procedia CIRP* 91 (2020) 290–294, <https://doi.org/10.1016/j.procir.2020.02.178>.
- [12] H. Bikas, A.K. Lianos, P. Stavropoulos, A design framework for additive manufacturing, *Int. J. Adv. Manuf. Technol.* 103 (2019) 3769–3783, <https://doi.org/10.1007/s00170-019-03627-z>.
- [13] J. Pakkanen, F. Calignano, F. Trevisan, M. Lorusso, E.P. Ambrosio, D. Manfredi, P. Fino, Study of internal channel surface roughnesses manufactured by selective laser melting in aluminum and titanium alloys, *Metall. Mater. Trans. A Phys. Metall. Mater. Sci.* 47 (2016) 3837–3844, <https://doi.org/10.1007/s11661-016-3478-7>.
- [14] G.A.O. Adam, D. Zimmer, On design for additive manufacturing: evaluating geometrical limitations, *Rapid Prototyp. J.* 21 (2015) 662–670, <https://doi.org/10.1108/RPJ-06-2013-0060>.
- [15] J. Kranz, D. Herzog, C. Emmelmann, J. Kranz, D. Herzog, Design guidelines for laser additive manufacturing of lightweight structures in TiAl6V4, *J. Laser Appl.* 27 (2015), S14001, <https://doi.org/10.2351/1.4885235>.
- [16] T. Schwanekamp, M. Bräuer, M. Reuber, Geometrical and topological potentialities and restrictions in selective laser sintering of customized carbide precision tools, *Proc. Lasers Manuf. Conf.* (2017).
- [17] M. Cloots, A.B. Spierings, K. Wegener, Assessing new support minimizing strategies for the additive manufacturing technology SLM, in: 24th Int. SFF Symp. Addit. Manuf. Conf., (2013).
- [18] R. Mertens, S. Clijsters, K. Kempen, J.P. Kruth, Optimization of scan strategies in selective laser melting of aluminum parts with downfacing areas, *J. Manuf. Sci. Eng. Trans. ASME* 136 (2014) 1–7, <https://doi.org/10.1115/1.4028620>.
- [19] D. Wang, Y. Yang, Z. Yi, X. Su, Research on the fabricating quality optimization of the overhanging surface in SLM process, *Int. J. Adv. Manuf. Technol.* 65 (2013) 1471–1484, <https://doi.org/10.1007/s00170-012-4271-4>.
- [20] D. Wang, S. Mai, D. Xiao, Y. Yang, Surface quality of the curved overhanging structure manufactured from 316-L stainless steel by SLM, *Int. J. Adv. Manuf. Technol.* 86 (2016) 781–792, <https://doi.org/10.1007/s00170-015-8216-6>.
- [21] J. Kruth, P. Mercelis, Feedback control of selective laser melting, *Proc. 3rd Int. Conf. Adv. Res. Virtual Rapid Prototyp.* (2007).
- [22] B. Vandenbroucke, J.P. Kruth, Selective laser melting of biocompatible metals for rapid manufacturing of medical parts, *Rapid Prototyp. J.* 13 (2007) 196–203, <https://doi.org/10.1108/13552540710776142>.
- [23] J.P. Kruth, L. Froyen, J. Van Vaerenbergh, P. Mercelis, M. Rombouts, B. Lauwers, Selective laser melting of iron-based powder, *J. Mater. Process. Technol.* 149 (2004) 616–622, <https://doi.org/10.1016/j.jmatprotec.2003.11.051>.
- [24] A.B. Spierings, M. Schneider, R. Eggenberger, Comparison of density measurement techniques for additive manufactured metallic parts, *Rapid Prototyp. J.* 17 (2011) 380–386, <https://doi.org/10.1108/13552541111156504>.
- [25] M. Cloots, L. Zumofen, A.B. Spierings, A. Kirchheim, K. Wegener, Approaches to minimize overhang angles of SLM parts, *Rapid Prototyp. J.* 23 (2017) 362–369, <https://doi.org/10.1108/RPJ-05-2015-0061>.
- [26] D.W. Rosen, Computer-aided design for additive manufacturing of cellular structures, *Comput. Aided Des. Appl.* 4 (2007) 585–594, <https://doi.org/10.1080/16864360.2007.10738493>.
- [27] P.N. Parkes, R. Butler, J. Meyer, A. de Oliveira, Static strength of metal-composite joints with penetrative reinforcement, *Compos. Struct.* 118 (2014) 250–256, <https://doi.org/10.1016/j.compstruct.2014.07.019>.
- [28] Y. Xiong, Y. Tang, S.-I. Park, D.W. Rosen, Harnessing process variables in additive manufacturing for design using manufacturing elements, *J. Mech. Des.* 142 (2020) 1–18, <https://doi.org/10.1115/1.4046069>.
- [29] P.N. Parkes, R. Butler, J. Meyer, A. de Oliveira, Static strength of metal-composite joints with penetrative reinforcement, *Compos. Struct.* 118 (2014) 250–256, <https://doi.org/10.1016/j.compstruct.2014.07.019>.
- [30] P. Maressa, L. Anodio, A. Bernasconi, A.G. Demir, B. Previtali, Effect of surface texture on the adhesion performance of laser treated Ti6Al4V alloy, *J. Adhes.* 91 (2014) 518–537, <https://doi.org/10.1080/00218464.2014.933809>.
- [31] B. Henriques, M. Sampaio, M. Buciumeanu, J.C.M. Souza, J.R. Gomes, F. Silva, O. Carvalho, Laser surface structuring of Ti6Al4V substrates for adhesion enhancement in Ti6Al4V-PEEK joints, *Mater. Sci. Eng. C* 79 (2017) 177–184, <https://doi.org/10.1016/j.msec.2017.04.157>.
- [32] Z. Feng, H. Zhao, C. Tan, B. Zhu, F. Xia, Q. Wang, B. Chen, X. Song, Effect of laser texturing on the surface characteristics and bonding property of 30CrMnSiA steel adhesive joints, *J. Manuf. Process.* 47 (2019) 219–228, <https://doi.org/10.1016/j.jmapro.2019.09.046>.
- [33] D.S. Robin, D. Arbelaez, S. Caspi, C. Sun, A. Sessler, W. Wan, M. Yoon, Superconducting toroidal combined-function magnet for a compact ion beam cancer therapy gantry, *Nucl. Instrum. Methods Phys. Res. Sect. A Accel. Spectrom. Detect. Assoc. Equip.* 659 (2011) 484–493, <https://doi.org/10.1016/j.nima.2011.08.049>.
- [34] S. Caspi, D. Arbelaez, L. Brouwer, D.R. Dietderich, H. Felice, R. Hafalia, S. Prestemon, D. Robin, C. Sun, W. Wan, A superconducting magnet mandrel with minimum symmetry laminations for proton therapy, *Nucl. Instrum. Methods Phys. Res. Sect. A Accel. Spectrom. Detect. Assoc. Equip.* 719 (2013) 44–49, <https://doi.org/10.1016/j.nima.2013.04.021>.
- [35] S. Caspi, D.R. Dietderich, P. Ferracin, N.R. Finney, M.J. Fuery, S.A. Gourlay, A. R. Hafalia, Design, fabrication, and test of a superconducting dipole magnet based on tilted solenoids, *IEEE Trans. Appl. Supercond.* 17 (2007) 2266–2269, <https://doi.org/10.1109/TASC.2007.899243>.
- [36] S. Graziosi, F. Cannazza, M. Vedani, A. Ratti, F. Tamburrino, M. Bordegoni, Design and testing of an innovative 3D-printed metal-composite junction, *Addit. Manuf.* 36 (2020), 101311, <https://doi.org/10.1016/j.addma.2020.101311>.
- [37] B. Auchmann, L. Brouwer, S. Caspi, J. Gao, G. Montenero, M. Negrazus, G. Rolando, S. Sanfilippo, Electromechanical design of a 16-T CCT twin-aperture dipole for FCC, *IEEE Trans. Appl. Supercond.* 28 (2018) 1–5, <https://doi.org/10.1109/TASC.2017.2772898>.
- [38] T. Larimian, M. Kannan, D. Grzesiak, B. AlMangour, T. Borkar, Effect of energy density and scanning strategy on densification, microstructure and mechanical properties of 316L stainless steel processed via selective laser melting, *Mater. Sci. Eng. A* 770 (2020), 138455, <https://doi.org/10.1016/j.msea.2019.138455>.
- [39] B. Leuteneker-Twelsiek, C. Klahn, M. Meboldt, Considering part orientation in design for additive manufacturing, *Procedia CIRP*, Elsevier B.V., 2016, pp. 408–413, <https://doi.org/10.1016/j.procir.2016.05.016>.
- [40] A. Schaub, B. Ahuja, L. Butzhammer, J. Osterziel, M. Schmidt, M. Merklein, Additive manufacturing of functional elements on sheet metal, *Phys. Procedia* 83 (2016) 797–807, <https://doi.org/10.1016/j.phpro.2016.08.082>.
- [41] L. Scime, J. Beuth, Using machine learning to identify in-situ melt pool signatures indicative of flaw formation in a laser powder bed fusion additive manufacturing process, *Addit. Manuf.* 25 (2019) 151–165, <https://doi.org/10.1016/j.addma.2018.11.010>.
- [42] M. Frascio, E.A. de Sousa Marques, R.J.C. Carbas, L.F.M. da Silva, M. Monti, M. Avalle, Review of tailoring methods for joints with additively manufactured adherends and adhesives, *Materials* 13 (2020), <https://doi.org/10.3390/ma13183949>.
- [43] H. Owen, A. Lomax, S. Jolly, Current and future accelerator technologies for charged particle therapy, *Nucl. Instrum. Methods Phys. Res. Sect. A Accel. Spectrom. Detect. Assoc. Equip.* 809 (2016) 96–104, <https://doi.org/10.1016/j.nima.2015.08.038>.